



A continuous surface tension force formulation for diffuse-interface models

Junseok Kim *

Department of Mathematics, 103 Multipurpose Science and Technology Building, University of California, Irvine, CA 92697-3875, USA

Received 25 March 2004; received in revised form 14 October 2004; accepted 19 October 2004
Available online 30 November 2004

Abstract

We present a new surface tension force formulation for a diffuse-interface model, which is derived for incompressible, immiscible Navier–Stokes equations separated by free interfaces. The classical infinitely thin boundary of separation between the two immiscible fluids is replaced by a transition region of small but finite width, across which the composition of the one of two fluids changes continuously. Various versions of diffuse-interface methods have been used successfully for the numerical simulations of two phase fluid flows. These methods are robust, efficient, and capable of computing interface singularities such as merging and pinching off. But prior studies used modified surface tension force formulations, therefore it is not straightforward to calculate pressure field because pressure includes the gradient terms resulting from the modified surface tension term. The new formulation allows us to calculate the pressure field directly from the governing equations. Computational results showing the accuracy and effectiveness of the method are given for a drop deformation and Rayleigh capillary instability.

© 2004 Elsevier Inc. All rights reserved.

Keywords: Continuum surface tension; Diffuse-interface; Phase field

1. Introduction

In this paper, we derive a new surface tension force formulation for a diffuse-interface model of incompressible, immiscible two-phase flow. The basic idea underlying the new formulation is to replace level set based surface tension formulation [7] by an equivalent phase field form. The diffuse-interface method (see the review paper [2] for the development and application of this model for both single-component and

* Tel.: +1 949 250 8993.

E-mail address: jskim@math.uci.edu.

URL: <http://www.math.uci.edu/~jskim>.

binary fluids) is getting the growing popularity in solving multiphase fluid flows especially when the interface undergoes extreme topological changes, e.g., merging or pinching off (see [4,17], and the references therein). In this method, we introduce an order parameter c , which is a mass fraction of one of two phases.

The advantages of this approach are: (1) topology changes without difficulties; interfaces can either merge or break up and no extra coding is required; (2) the composition field c has physical meanings not only on the interface but also in the bulk phases. Therefore, this method can be applied to many physical phase states such as miscible, immiscible, partially miscible, lamellar phases, to name a few. Fig. 1 shows evolution of the randomly oriented lamellar structure of block copolymers under steady shear flow [16]; (3) it can be naturally extended to multicomponent systems (more than two components, e.g., ternary system) and three space dimensions with straightforward manner [18]. Fig. 2 shows time sequence of two droplets leaving interfaces under surface tension forces. This system consists of three immiscible, density matched fluids, i.e., top and bottom fluid (I), middle fluid (II), and two droplets (III) between interfaces. Surface tension between fluid I and III are greater than the other ones.

The continuum surface force (CSF) formulation [6] is widely used in modeling surface tension force of two phase fluid flows in volume-of-fluid (VOF) [10,11,26,32], level set method [7], and diffuse-interface method [4,9]. In the CSF computational model, the surface tension is converted into a form of volume force and the resulting force is proportional to the product of the interface gradient and the surface curvature. The effects of surface tension are consequently included in the computational model through an external forcing term added to the momentum equation.

In a level set method [7], the governing equation for the fluid velocity, \mathbf{u} and the pressure, p can be written as

$$\rho(\phi)(\mathbf{u}_t + \mathbf{u} \cdot \nabla \mathbf{u}) = -\nabla p + \nabla \cdot (2\eta(\phi)\mathbf{D}) - \sigma\kappa(\phi)\delta(\phi)\nabla\phi + \rho(\phi)\mathbf{g}, \tag{1}$$

where ρ , η , $\mathbf{D} = (\nabla\mathbf{u} + \nabla\mathbf{u}^T)/2$, σ , κ , δ , and \mathbf{g} are the density, the viscosity, the deformation tensor, the surface tension coefficient, the curvature, the Dirac delta function, and the gravity, respectively. The level set function is denoted as ϕ and it is taken positive in one phase and negative in the other phase. Therefore, the

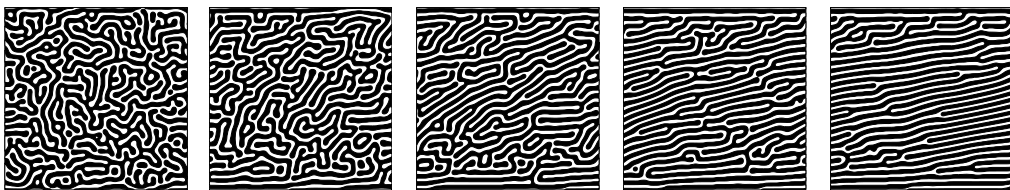


Fig. 1. Evolution of the lamellar structure under shear flow.

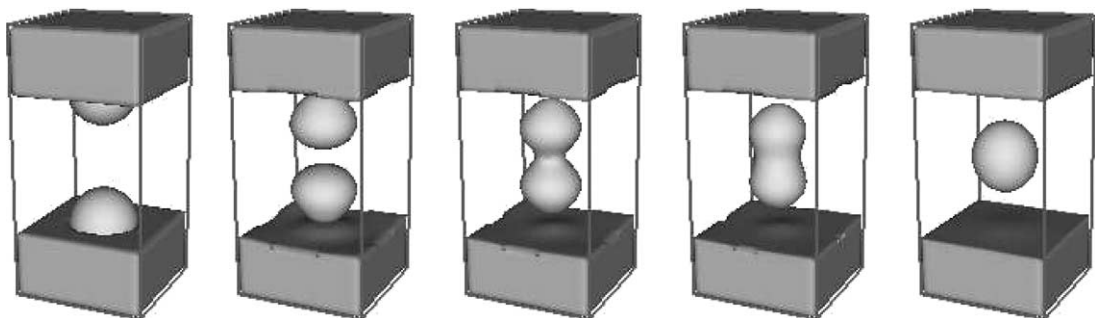


Fig. 2. Evolution of two droplets leaving interfaces under surface tension forces.

interface of two fluids is the zero level set of ϕ . Also, ϕ is initialized to be the signed normal distance from the interface. For simplicity of presentation, here we focus on density (which is taken to be 1) and viscosity matched case. In the last example, we will present a bubble rising in the water to validate our scheme to the case having large density and viscosity ratios. Then Eq. (1) becomes

$$\mathbf{u}_t + \mathbf{u} \cdot \nabla \mathbf{u} = -\nabla p + \eta \Delta \mathbf{u} - \sigma \kappa(\phi) \delta(\phi) \nabla \phi.$$

In a diffuse-interface method [4,9], the governing equation can be written as

$$\mathbf{u}_t + \mathbf{u} \cdot \nabla \mathbf{u} = -\nabla p + \eta \Delta \mathbf{u} + \mathbf{F}_i, \quad \text{for } i = 1, 2, \text{ or } 3. \quad (2)$$

Here

$$\mathbf{F}_1 = \sigma \epsilon \alpha \nabla \cdot (|\nabla c|^2 I - \nabla c \otimes \nabla c), \quad (3)$$

$$\mathbf{F}_2 = \frac{\sigma \alpha}{\epsilon} \mu \nabla c, \quad (4)$$

$$\mathbf{F}_3 = -\frac{\sigma \alpha}{\epsilon} c \nabla \mu, \quad (5)$$

where α is given in Eq. (14), ϵ is a small positive parameter, I is the unit tensor δ_{ij} , μ is a chemical potential, which is defined as

$$\mu = F'(c) - \epsilon^2 \Delta c, \quad (6)$$

where $F(c) = \frac{1}{4} c^2 (1 - c)^2$. The term $\nabla c \otimes \nabla c$ is the usual tensor product, i.e. $(\nabla c \otimes \nabla c)_{ij} = \frac{\partial c}{\partial x_i} \frac{\partial c}{\partial x_j}$. In [15,19–22,27], surface tension formulation \mathbf{F}_1 is used. In [3,9,12,34], \mathbf{F}_2 is used. \mathbf{F}_3 is used in [13,14,17]. In this paper, we propose a new surface tension force formulation, \mathbf{F}_4 .

$$\mathbf{F}_4 = -\sigma \nabla \cdot \left(\frac{\nabla c}{|\nabla c|} \right) \epsilon \alpha |\nabla c|^2 \frac{\nabla c}{|\nabla c|}, \quad (7)$$

where $\nabla \cdot \left(\frac{\nabla c}{|\nabla c|} \right)$, $\epsilon \alpha |\nabla c|^2$, and $\frac{\nabla c}{|\nabla c|}$ correspond to $\kappa(\phi)$, $\delta(\phi)$, and $\nabla \phi$ in Eq. (1), respectively. This new formulation idea is from the level set formulation.

The curvature of each level set is

$$\kappa = \nabla \cdot \left(\frac{\nabla c}{|\nabla c|} \right) = \frac{1}{|\nabla c|} \left(\Delta c - \nabla \nabla c : \frac{\nabla c}{|\nabla c|} \otimes \frac{\nabla c}{|\nabla c|} \right), \quad (8)$$

where the operator ‘:’ is defined as $A : B = \sum_{ij} a_{ij} b_{ij}$. Therefore the Eqs. (3)–(5) can be rewritten as

$$\begin{aligned} \mathbf{F}_1 &= \sigma \epsilon \alpha \nabla \cdot (|\nabla c|^2 I - \nabla c \otimes \nabla c) = \sigma \epsilon \alpha \left(-\Delta c \nabla c + \frac{1}{2} \nabla |\nabla c|^2 \right) \\ &= \mathbf{F}_4 - \sigma \alpha \epsilon \left[\left(\nabla \nabla c : \frac{\nabla c}{|\nabla c|} \otimes \frac{\nabla c}{|\nabla c|} \right) \nabla c - \frac{1}{2} \nabla |\nabla c|^2 \right], \end{aligned} \quad (9)$$

$$\begin{aligned} \mathbf{F}_2 &= \frac{\sigma \alpha}{\epsilon} \mu \nabla c = -\sigma \alpha \epsilon \kappa |\nabla c| \nabla c + \sigma \alpha \left(\frac{f(c)}{\epsilon} - \epsilon \nabla \nabla c : \frac{\nabla c}{|\nabla c|} \otimes \frac{\nabla c}{|\nabla c|} \right) \nabla c \\ &= \mathbf{F}_4 + \sigma \alpha \left(\frac{f(c)}{\epsilon} - \epsilon \nabla \nabla c : \frac{\nabla c}{|\nabla c|} \otimes \frac{\nabla c}{|\nabla c|} \right) \nabla c, \end{aligned} \quad (10)$$

$$\mathbf{F}_3 = -\frac{\sigma \alpha}{\epsilon} c \nabla \mu = \frac{\sigma \alpha}{\epsilon} (\mu \nabla c - \nabla(c\mu)) = \mathbf{F}_4 + \sigma \alpha \left(\frac{f(c)}{\epsilon} - \epsilon \nabla \nabla c : \frac{\nabla c}{|\nabla c|} \otimes \frac{\nabla c}{|\nabla c|} \right) \nabla c - \frac{\sigma \alpha}{\epsilon} \nabla(c\mu). \quad (11)$$

The previous numerical studies [3,9,12–15,19–22,27,34] with \mathbf{F}_1 , \mathbf{F}_2 , or \mathbf{F}_3 did not calculate pressure field explicitly. It is evident from the above equations (9)–(11) that why previous works did not calculate pressure field explicitly. It is partly due to the fact that all the pure gradient terms are absorbed in the pressure in the formulations \mathbf{F}_1 , \mathbf{F}_2 , or \mathbf{F}_3 .

Calculation of pressure field is important in some situations. For example, a circular hydraulic jump is formed when a vertical liquid jet impinges on a horizontal surface and spreads out radially on the surface. In a study [35], they found that the pressure deviation from the hydrostatic equilibrium around the hydraulic jump is essential for the structure formation and that the surface tension plays an important role for the establishment of the pressure deviation.

For another example, let us consider a biomedical simulation which is one of the most important applications of computational fluid dynamics. The growth of the vascularized tumor depends vitally on the nutrient transfer rate, the level of nutrient in the blood, and the blood pressure in the new capillaries. The phase-field model for the sharp interfaced model [36] of a tumor growth can be written as

$$\mathbf{u} - \bar{\epsilon}\Delta\mathbf{u} = -\bar{\mu}\nabla p - \mathbf{F}_{sf}, \tag{12}$$

where $\bar{\epsilon}$ is a constant, $\bar{\mu}$ is cell mobility, and \mathbf{F}_{sf} is a surface tension force. The authors in the paper [36] tested the pressure field with the new surface tension force \mathbf{F}_4 and found a good agreement with the results from the sharp interface model. The pressure field plays a key role in explaining the rate of nutrient transfer, and hence the rate of growth of the tumor [36].

Here, we view the diffuse-interface model as a computational method. The most significant computational advantage of this method is that explicit tracking of the interface is unnecessary. Note that only the 1/2 level set of the concentration field is physically relevant as interface locations unlike most other diffuse-interface models. This proposed diffuse-interface model is a hybrid method which combines a level set type surface tension force formulation and a concentration relaxation by a diffuse-interface model.

The main purpose of this paper is to introduce a new surface tension force formulation in diffuse-interface models. The novel feature of this new formulation is that it permits the explicit calculation of pressure field from the governing equations. The contents of this paper are: in Section 2 we discretize the new surface tension force formulation. In Section 4 we present numerical experiments to validate our new surface tension formulation. The experiments are simulations of 2 dimensional drop, 3 dimensional drop under shear flow, and axisymmetric thread breakup under capillary force. In Section 5, conclusions are given.

2. Discretization of the surface tension force formulation

In this section, we derive a discretization of the new surface tension force and for simplicity, we present it in 2D and 3D case is a straightforward extension. Let the surface tension formulation (7) be rewritten as

$$\mathbf{F}_4 = -\sigma\epsilon\alpha\nabla \cdot \left(\frac{\nabla c}{|\nabla c|} \right) |\nabla c| \nabla c. \tag{13}$$

We want the concentration field, c , to be locally equilibrium state during evolution. To match the surface tension of the sharp interface model, α must satisfy

$$\epsilon\alpha \int_{-\infty}^{\infty} (c_x^{eq})^2 dx = 1, \tag{14}$$

where $c^{eq}(x,y) = [1 + \tanh(x/(2\sqrt{2}\epsilon))]/2$ is an equilibrium composition profile in the infinite domain when the chemical potential is given as Eq. (6) [14] and it is a good approximation in the finite domain. Therefore from Eq. (14), we get $\alpha = 6\sqrt{2}$.

Let a computational domain be partitioned in Cartesian geometry into a uniform mesh with mesh spacing h . The center of each cell, Ω_{ij} , is located at $(x_{ij}, y_{ij}) = ((i - 0.5)h, (j - 0.5)h)$ for $i = 1, \dots, M$ and $j = 1, \dots, N$. M and N are the numbers of cells in x and y -directions, respectively. The cell vertices are located at $(x_{i+\frac{1}{2},j+\frac{1}{2}}, y_{i+\frac{1}{2},j+\frac{1}{2}}) = (ih, jh)$. Vertex-centered normal vectors are obtained by differentiating the phase field in the four surrounding cells. For example, the normal vector at the top right vertex of cell Ω_{ij} is given by

$$\mathbf{n}_{i+\frac{1}{2},j+\frac{1}{2}} = \left(n_{i+\frac{1}{2},j+\frac{1}{2}}^x, n_{i+\frac{1}{2},j+\frac{1}{2}}^y \right) = \left(\frac{c_{i+1,j} + c_{i+1,j+1} - c_{ij} - c_{i,j+1}}{2h}, \frac{c_{i,j+1} + c_{i+1,j+1} - c_{ij} - c_{i+1,j}}{2h} \right).$$

The curvature (8) is calculated at cell centers from the vertex-centered normals and is given by

$$\kappa(c_{ij}) = \nabla_d \cdot \left(\frac{\mathbf{n}}{|\mathbf{n}|} \right)_{ij} = \frac{1}{2h} \left(\frac{n_{i+\frac{1}{2},j+\frac{1}{2}}^x + n_{i+\frac{1}{2},j+\frac{1}{2}}^y}{|\mathbf{n}_{i+\frac{1}{2},j+\frac{1}{2}}|} + \frac{n_{i+\frac{1}{2},j-\frac{1}{2}}^x - n_{i+\frac{1}{2},j-\frac{1}{2}}^y}{|\mathbf{n}_{i+\frac{1}{2},j-\frac{1}{2}}|} - \frac{n_{i-\frac{1}{2},j+\frac{1}{2}}^x - n_{i-\frac{1}{2},j+\frac{1}{2}}^y}{|\mathbf{n}_{i-\frac{1}{2},j+\frac{1}{2}}|} - \frac{n_{i-\frac{1}{2},j-\frac{1}{2}}^x + n_{i-\frac{1}{2},j-\frac{1}{2}}^y}{|\mathbf{n}_{i-\frac{1}{2},j-\frac{1}{2}}|} \right),$$

where ∇_d is a finite difference approximation to the divergence operator. And the cell-centered normal is the average of vertex normals,

$$\nabla_d c_{ij} = \left(\mathbf{n}_{i+\frac{1}{2},j+\frac{1}{2}} + \mathbf{n}_{i+\frac{1}{2},j-\frac{1}{2}} + \mathbf{n}_{i-\frac{1}{2},j+\frac{1}{2}} + \mathbf{n}_{i-\frac{1}{2},j-\frac{1}{2}} \right) / 4,$$

where ∇_d is a finite difference approximation to the gradient operator. Therefore, the discretization of the proposed surface tension force formulation \mathbf{F}_4 is

$$\mathbf{F}_4(c_{ij}) = -\sigma\epsilon\alpha \nabla_d \cdot \left(\frac{\mathbf{n}}{|\mathbf{n}|} \right)_{ij} |\nabla_d c_{ij}| \nabla_d c_{ij}.$$

3. Numerical experiment without flow

Let us consider equilibrium of a drop placed within another fluid. Let the drop composition be defined as

$$c(x,y) = \frac{1}{2} \left(1 + \tanh \frac{1 - \sqrt{x^2 + y^2}}{2\sqrt{2}\epsilon} \right). \tag{15}$$

We define the interface location to be the position of the level set $c = 0.5$. Fig. 3(a) shows composition field (15) of an unit circle along with the interface (solid line).

In equilibrium state of a droplet, velocity vanishes ($\mathbf{u} \equiv 0$) and therefore the governing Eq. (2) reduces to Eq. (16) and therefore pressure gradient should balance surface tension force.

$$\nabla p = -\sigma\epsilon\alpha \left[\nabla \cdot \left(\frac{\nabla c}{|\nabla c|} \right) |\nabla c| \nabla c \right]. \tag{16}$$

We solve Eq. (17) numerically by taking divergence operator to Eq. (16) with $\sigma = 1$, 256×256 mesh, computational domain $\Omega = [-4,4] \times [-4,4]$, and $\epsilon = 0.03$.

$$\Delta p = -\sigma\epsilon\alpha \nabla \cdot \left[\nabla \cdot \left(\frac{\nabla c}{|\nabla c|} \right) |\nabla c| \nabla c \right], \tag{17}$$

where we discretize Δp by

$$\Delta p_{i+\frac{1}{2},j+\frac{1}{2}} = (p_{i-\frac{1}{2},j+\frac{3}{2}} + p_{i+\frac{1}{2},j+\frac{3}{2}} + p_{i+\frac{3}{2},j+\frac{3}{2}} + p_{i-\frac{1}{2},j+\frac{1}{2}} - 8p_{i+\frac{1}{2},j+\frac{1}{2}} + p_{i+\frac{3}{2},j+\frac{1}{2}} + p_{i-\frac{1}{2},j-\frac{1}{2}} + p_{i+\frac{1}{2},j-\frac{1}{2}} + p_{i+\frac{3}{2},j-\frac{1}{2}}) / (3h^2).$$

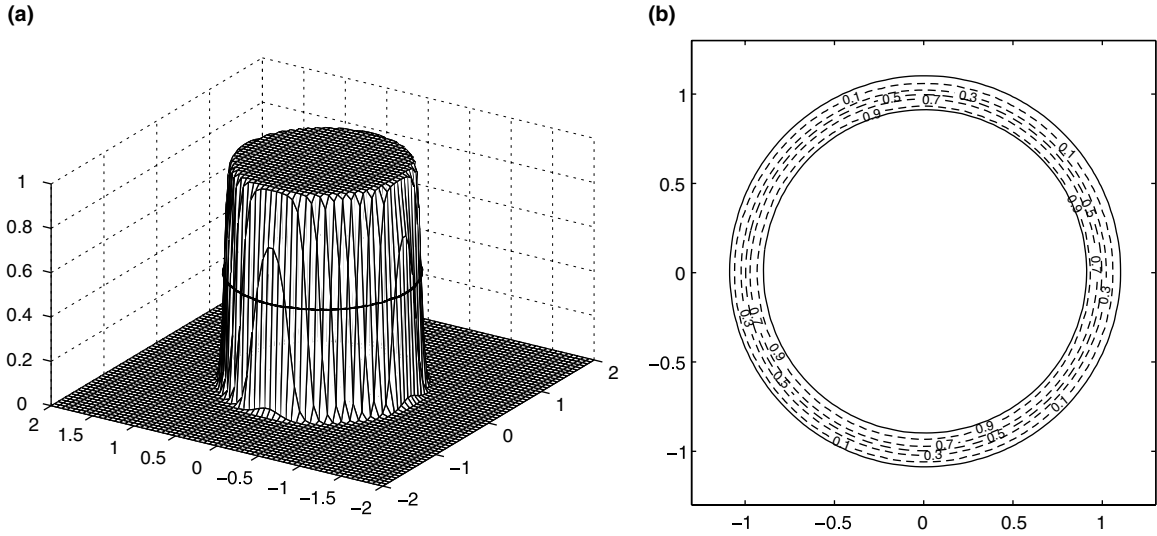


Fig. 3. (a) Composition field along with contour plot $c(x,y) = 0.5$. (b) Contour plots of pressure field.

From Laplace’s formulation we can obtain the theoretical prediction of the pressure-jump inside an infinite cylinder as $\Delta p_{\text{theor}} = \sigma/R$, where σ is surface tension coefficient and R is the cylinder radius. Fig. 3(b) shows isocontour of the pressure field at $(p = 0.1, 0.3, 0.5, 0.7, 0.9)$ along with composition (solid circles) at $c = 0.1$ and 0.9 . Pressure changes within interface region and Laplace’s law is well verified.

Fig. 4(a) shows numerically calculated curvature around interface region along with the exact one, ‘ \circ ’, defined by $\nabla \cdot (\nabla c/|\nabla c|)$ on the ellipsoid $\frac{x^2}{4} + y^2 = 1$ (solid line). Fig. 4(b) shows contour plots (dotted lines) of the pressure field around the ellipsoid $\frac{x^2}{4} + y^2 = 1$ (solid line).

4. Numerical experiments with flow

In this section we present 2D, 3D, and axisymmetric flow simulations to demonstrate the flexibility and accuracy of the new surface tension formulation. For completeness, we describe numerical solution procedure for 2D. 3D is straightforward extension and axisymmetric case is given in detail in [15]. The nondimensional governing equations, Navier–Stokes–Cahn–Hilliard equations (NSCH), are

$$\nabla \cdot \mathbf{u} = 0, \tag{18}$$

$$\mathbf{u}_t + \mathbf{u} \cdot \nabla \mathbf{u} = -\nabla p + \frac{1}{Re} \nabla \cdot [\eta(c)(\nabla \mathbf{u} + \nabla \mathbf{u}^T)] - \frac{\epsilon \alpha}{We} \nabla \cdot \left(\frac{\nabla c}{|\nabla c|} \right) |\nabla c| \nabla c, \tag{19}$$

$$c_t + \mathbf{u} \cdot \nabla c = \frac{1}{Pe} \nabla \cdot (M(c) \nabla \mu), \tag{20}$$

$$\mu = f(c) - C \Delta c, \tag{21}$$

where the dimensionless parameters are Reynolds number, $Re = \rho_* V_* L_* / \eta_*$, Weber number, $We = \rho_* L_* V_*^2 / \sigma$, Cahn number, $C = \epsilon^2 / \mu_*$, and diffusional Peclet number, $Pe = L_* V_* / (M_* \mu_*)$. The values with lower * are characteristic values of corresponding ones. $M(c)$ is a composition dependent mobility and is defined by $M(c) = c(1 - c)$ [8].

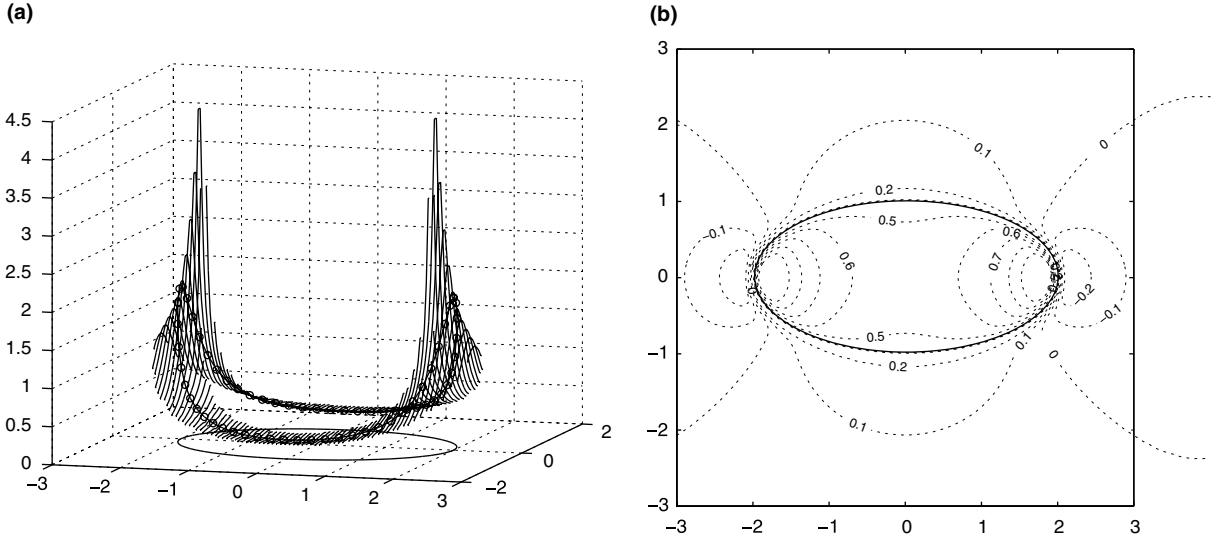


Fig. 4. (a) Numerically calculated curvature around interface region along with the exact one ‘o’ on the ellipsoid $\frac{x^2}{4} + y^2 = 1$ (solid line). (b) Contour plots (dotted line) of pressure field around the ellipsoid $\frac{x^2}{4} + y^2 = 1$ (solid line).

4.1. Numerical procedure

Our strategy for solving the system (18)–(21) is a fractional step scheme having two parts: first we solve the momentum and composition equations (19)–(21) without strictly enforcing the incompressibility constraint (18), then we approximately project the resulting velocity field onto the space of discretely divergence-free vector fields [5].

The discrete velocity field \mathbf{u}_{ij}^n and composition field c_{ij}^n are located at cell centers. The pressure $p_{i+\frac{1}{2},j+\frac{1}{2}}^{n-\frac{1}{2}}$ is located at cell corners. The notation \mathbf{u}_{ij}^n is used to represent an approximation to $\mathbf{u}(x_i, y_j, t^n)$, where $t^n = n\Delta t$ and Δt is a time step. Likewise, $p_{i+\frac{1}{2},j+\frac{1}{2}}^{n-\frac{1}{2}}$ is an approximation to $p(x_i + \frac{h}{2}, y_j + \frac{h}{2}, t^n - \frac{\Delta t}{2})$.

The time-stepping procedure is based on the Crank–Nicholson type method. At the beginning of each time step, given $\mathbf{u}^{n-1}, \mathbf{u}^n, c^{n-1}, c^n$, and $p^{n-\frac{1}{2}}$, we want to find $\mathbf{u}^{n+1}, c^{n+1}$, and $p^{n+\frac{1}{2}}$ which solve the following second-order temporal discretization of the equation of motion:

$$\begin{aligned} \frac{\mathbf{u}^{n+1} - \mathbf{u}^n}{\Delta t} &= -\nabla_d p^{n+\frac{1}{2}} + \frac{1}{2Re} \nabla_d \cdot \eta(c^{n+1}) [\nabla_d \mathbf{u}^{n+1} + (\nabla_d \mathbf{u}^{n+1})^T] + \frac{1}{2Re} \nabla_d \cdot \eta(c^n) [\nabla_d \mathbf{u}^n + (\nabla_d \mathbf{u}^n)^T] \\ &\quad + \mathbf{F}^{n+\frac{1}{2}} - (\mathbf{u} \cdot \nabla_d \mathbf{u})^{n+\frac{1}{2}}, \\ \frac{c^{n+1} - c^n}{\Delta t} &= \frac{1}{Pe} \nabla_d \cdot (M(c^{n+\frac{1}{2}}) \nabla_d \mu^{n+\frac{1}{2}}) - (\mathbf{u} \cdot \nabla_d c)^{n+\frac{1}{2}}, \end{aligned} \quad (22)$$

$$\mu^{n+\frac{1}{2}} = \frac{1}{2} [f(c^n) + f(c^{n+1})] - \frac{C}{2} \Delta_d (c^n + c^{n+1}), \quad (23)$$

where $\mathbf{F}^{n+\frac{1}{2}}$ is the surface tension force term and the updated flow field satisfies the incompressibility condition

$$\nabla_d \cdot \mathbf{u}^{n+1} = 0.$$

The outline of the main procedures in one time step is as follows.

- Step 1. Initialize c^0 to be the locally equilibrated composition profile and \mathbf{u}^0 to be the divergence-free velocity field.
- Step 2. The half time values $\mathbf{u}^{n+\frac{1}{2}}$ and $c^{n+\frac{1}{2}}$ are calculated using an extrapolation from previous values, i.e., $\mathbf{u}^{n+\frac{1}{2}} = (3\mathbf{u}^n - \mathbf{u}^{n-1})/2$ and $c^{n+\frac{1}{2}} = (3c^n - c^{n-1})/2$. With these half time values, we calculate $(\mathbf{u} \cdot \nabla_d c)^{n+\frac{1}{2}}$ by using a second order ENO scheme [28].
- Step 3. Update the composition field c^n to c^{n+1} by solving the discrete Cahn–Hilliard (CH) Eqs. (22) and (23). Details of this step, which use a nonlinear multigrid method and a second order accurate discretization in time and space, are presented in Section 4.1.1. Once c^{n+1} is obtained, we compute $c^{n+\frac{1}{2}} = (c^n + c^{n+1})/2$ and $\eta(c^{n+\frac{1}{2}})$.
- Step 4. Compute $(\mathbf{u} \cdot \nabla_d \mathbf{u})^{n+\frac{1}{2}}$ by using a second order ENO scheme and $\mathbf{F}^{n+\frac{1}{2}}$ with $c^{n+\frac{1}{2}}$.
- Step 5. We solve

$$\frac{\mathbf{u}^* - \mathbf{u}^n}{\Delta t} = -\nabla_d p^{n-\frac{1}{2}} + \frac{1}{2Re} \nabla_d \cdot \eta(c^{n+1}) [\nabla_d \mathbf{u}^* + (\nabla_d \mathbf{u}^*)^T] + \frac{1}{2Re} \nabla_d \cdot \eta(c^n) [\nabla_d \mathbf{u}^n + (\nabla_d \mathbf{u}^n)^T] + \mathbf{F}^{n+\frac{1}{2}} - (\mathbf{u} \cdot \nabla_d \mathbf{u})^{n+\frac{1}{2}} \tag{24}$$

using a multigrid method for the intermediate velocity \mathbf{u}^* without strictly enforcing the incompressibility constraint.

- Step 6. Project \mathbf{u}^* onto the space of discretely divergence-free vector fields and get the velocity \mathbf{u}^{n+1} , i.e., $\mathbf{u}^* = \mathbf{u}^{n+1} + \Delta t \nabla_d \phi$, where ϕ satisfies $\Delta_d \phi = \nabla_d \cdot \frac{\mathbf{u}^* - \mathbf{u}^n}{\Delta t}$.
- Step 7. Update pressure, $p^{n+\frac{1}{2}} = p^{n-\frac{1}{2}} + \phi$. These complete one time step.

4.1.1. Cahn–Hilliard equation with advection – a nonlinear multigrid method

In this section, we describe a nonlinear full approximation storage (FAS) multigrid method to solve the nonlinear discrete system (22) and (23) at the implicit time level. The nonlinearity is treated using one step of Newton’s iteration and a pointwise Gauss–Seidel relaxation scheme is used as the smoother in the multigrid method. See the reference text [33] for additional details and background. The algorithm of the nonlinear multigrid method for solving the discrete CH system is:

First, let us rewrite Eqs. (22) and (23) as follows.

$$\text{NSO}(c^{n+1}, \mu^{n+\frac{1}{2}}) = (\phi^n, \psi^n),$$

where

$$\text{NSO}(c^{n+1}, \mu^{n+\frac{1}{2}}) = \left(\frac{c^{n+1}}{\Delta t} - \frac{1}{Pe} \nabla_d \cdot (M(c^{n+\frac{1}{2}}) \nabla_d \mu^{n+\frac{1}{2}}), \mu^{n+\frac{1}{2}} - \frac{1}{2} f(c^{n+1}) + \frac{C}{2} \Delta_d c^{n+1} \right)$$

and the source term is $(\phi^n, \psi^n) = (\frac{c^n}{\Delta t} - (\mathbf{u} \cdot \nabla_d c)^{n+\frac{1}{2}}, \frac{1}{2} f(c^n) - \frac{C}{2} \Delta_d c^n)$.

In the following description of one FAS cycle, we assume a sequence of grids Ω_k (Ω_{k-1} is coarser than Ω_k by factor 2). Given the number ν of pre- and post-smoothing relaxation sweeps, an iteration step for the nonlinear multigrid method using the V-cycle is formally written as follows [33]:

4.1.1.1. FAS multigrid cycle.

$$\left\{ c_k^{m+1}, \mu_k^{m+\frac{1}{2}} \right\} = \text{FAScycle} \left(k, c_k^m, \mu_k^{m-\frac{1}{2}}, \text{NSO}_k, \phi_k^m, \psi_k^m, \nu \right).$$

That is, $\left\{ c_k^m, \mu_k^{m-\frac{1}{2}} \right\}$ and $\left\{ c_k^{m+1}, \mu_k^{m+\frac{1}{2}} \right\}$ are the approximations of $c^{n+1}(x_i, y_j)$ and $\mu^{n+\frac{1}{2}}(x_i, y_j)$ before and after an FAScycle. Now, define the FAScycle.

(1) *Presmoothing*

$$\left\{ \bar{c}_k^m, \bar{\mu}_k^{m-\frac{1}{2}} \right\} = \text{SMOOTH}^v \left(c_k^n, c_k^m, \mu_k^{m-\frac{1}{2}}, \text{NSO}_k, \phi_k^n, \psi_k^n \right),$$

which means performing v smoothing steps with the initial approximations $c_k^m, \mu_k^{m-\frac{1}{2}}, c_k^n$, source terms ϕ_k^n, ψ_k^n , and SMOOTH relaxation operator to get the approximations $\bar{c}_k^m, \bar{\mu}_k^{m-\frac{1}{2}}$. One SMOOTH relaxation operator step consists of solving the system (27) and (28) given below by 2×2 matrix inversion for each i and j . Here, we derive the smoothing operator in two dimensions. Rewriting Eq. (22), we get

$$\frac{c_{ij}^{n+1}}{\Delta t} + \frac{M_{i+\frac{1}{2},j}^{n+\frac{1}{2}} + M_{i-\frac{1}{2},j}^{n+\frac{1}{2}} + M_{i,j+\frac{1}{2}}^{n+\frac{1}{2}} + M_{i,j-\frac{1}{2}}^{n+\frac{1}{2}}}{h^2 Pe} \mu_{ij}^{n+\frac{1}{2}} = \phi_{ij}^n + \frac{M_{i+\frac{1}{2},j}^{n+\frac{1}{2}} \mu_{i+1,j}^{n+\frac{1}{2}} + M_{i-\frac{1}{2},j}^{n+\frac{1}{2}} \mu_{i-1,j}^{n+\frac{1}{2}} + M_{i,j+\frac{1}{2}}^{n+\frac{1}{2}} \mu_{i,j+1}^{n+\frac{1}{2}} + M_{i,j-\frac{1}{2}}^{n+\frac{1}{2}} \mu_{i,j-1}^{n+\frac{1}{2}}}{h^2 Pe}. \tag{25}$$

Since $f(c_{ij}^{n+1})$ is nonlinear with respect to c_{ij}^{n+1} , we linearize $f(c_{ij}^{n+1})$ at c_{ij}^m , i.e.,

$$f(c_{ij}^{n+1}) \approx f(c_{ij}^m) + \frac{df(c_{ij}^m)}{dc} (c_{ij}^{n+1} - c_{ij}^m).$$

After substitution of this into (23), we get

$$-\left(\frac{2C}{h^2} + \frac{df(c_{ij}^m)}{2dc} \right) c_{ij}^{n+1} + \mu_{ij}^{n+\frac{1}{2}} = \psi_{ij}^n + \frac{1}{2} f(c_{ij}^m) - \frac{df(c_{ij}^m)}{2dc} c_{ij}^m - \frac{C}{2h^2} (c_{i+1,j}^{n+1} + c_{i-1,j}^{n+1} + c_{i,j+1}^{n+1} + c_{i,j-1}^{n+1}). \tag{26}$$

Next, we replace c_{kl}^{n+1} and $\mu_{kl}^{n+\frac{1}{2}}$ in the Eqs. (25) and (26) with \bar{c}_{kl}^m and $\bar{\mu}_{kl}^{m-\frac{1}{2}}$ if $k \leq i$ and $l \leq j$, otherwise with c_{kl}^m and $\mu_{kl}^{m-\frac{1}{2}}$, i.e.,

$$\frac{\bar{c}_{ij}^m}{\Delta t} + \frac{M_{i+\frac{1}{2},j}^{m-\frac{1}{2}} + M_{i-\frac{1}{2},j}^{m-\frac{1}{2}} + M_{i,j+\frac{1}{2}}^{m-\frac{1}{2}} + M_{i,j-\frac{1}{2}}^{m-\frac{1}{2}}}{h^2 Pe} \bar{\mu}_{ij}^{m-\frac{1}{2}} = \phi_{ij}^n + \frac{M_{i+\frac{1}{2},j}^{m-\frac{1}{2}} \mu_{i+1,j}^{m-\frac{1}{2}} + M_{i-\frac{1}{2},j}^{m-\frac{1}{2}} \bar{\mu}_{i-1,j}^{m-\frac{1}{2}} + M_{i,j+\frac{1}{2}}^{m-\frac{1}{2}} \mu_{i,j+1}^{m-\frac{1}{2}} + M_{i,j-\frac{1}{2}}^{m-\frac{1}{2}} \bar{\mu}_{i,j-1}^{m-\frac{1}{2}}}{h^2 Pe}, \tag{27}$$

where $M_{i+\frac{1}{2},j}^{m-\frac{1}{2}} = M((c_{ij}^m + c_{i+1,j}^m + c_{ij}^n + c_{i+1,j}^n)/4)$ and the other terms are similarly defined.

$$-\left(\frac{2C}{h^2} + \frac{df(c_{ij}^m)}{2dc} \right) \bar{c}_{ij}^m + \bar{\mu}_{ij}^{m-\frac{1}{2}} = \psi_{ij}^n + \frac{1}{2} f(c_{ij}^m) - \frac{df(c_{ij}^m)}{2dc} c_{ij}^m - \frac{C}{2h^2} (c_{i+1,j}^m + \bar{c}_{i-1,j}^m + c_{i,j+1}^m + \bar{c}_{i,j-1}^m). \tag{28}$$

(2) *Compute the defect*

$$(\bar{d}_{1k}^m, \bar{d}_{2k}^m) = (\phi_k^n, \psi_k^n) - \text{NSO}_k(\bar{c}_k^m, \bar{\mu}_k^{m-\frac{1}{2}}). \tag{29}$$

(3) *Restrict the defect and* $\left\{ \bar{c}_k^m, \bar{\mu}_k^{m-\frac{1}{2}} \right\}$

$$(\bar{d}_{1k-1}^m, \bar{d}_{2k-1}^m) = I_k^{k-1}(\bar{d}_{1k}^m, \bar{d}_{2k}^m), (\bar{d}_{k-1}^m, \bar{\mu}_{k-1}^{m-\frac{1}{2}}) = I_k^{k-1}(\bar{c}_k^m, \bar{\mu}_k^{m-\frac{1}{2}}).$$

The restriction operator I_k^{k-1} maps k -level functions to $(k - 1)$ -level functions.

$$d_{k-1}(x_i, y_j) = I_k^{k-1} d_k(x_i, y_j) = \frac{1}{4} [d_k(x_{i-\frac{1}{2}}, y_{j-\frac{1}{2}}) + d_k(x_{i-\frac{1}{2}}, y_{j+\frac{1}{2}}) + d_k(x_{i+\frac{1}{2}}, y_{j-\frac{1}{2}}) + d_k(x_{i+\frac{1}{2}}, y_{j+\frac{1}{2}})].$$

(4) *Compute the right-hand side*

$$(\phi_{k-1}^n, \psi_{k-1}^n) = (\bar{d}_{1k-1}^m, \bar{d}_{2k-1}^m) + \text{NSO}_{k-1}(\bar{c}_{k-1}^m, \bar{\mu}_{k-1}^{m-\frac{1}{2}}).$$

(5) *Compute an approximate solution* $\left\{ \hat{c}_{k-1}^m, \hat{\mu}_{k-1}^{m-\frac{1}{2}} \right\}$ *of the coarse grid equation on* Ω_{k-1} , *i.e.*

$$\text{NSO}_{k-1}(c_{k-1}^m, \mu_{k-1}^{m-\frac{1}{2}}) = (\phi_{k-1}^n, \psi_{k-1}^n). \tag{30}$$

If $k = 1$, we explicitly invert a 2×2 matrix to obtain the solution. If $k > 1$, we solve (30) by performing a FAS k -grid cycle using $\{\bar{c}_{k-1}^m, \bar{\mu}_{k-1}^{m-\frac{1}{2}}\}$ as an initial approximation:

$$\{\hat{c}_{k-1}^m, \hat{\mu}_{k-1}^{m-\frac{1}{2}}\} = \text{FAScycle}(k-1, c_{k-1}^n, \bar{c}_{k-1}^m, \bar{\mu}_{k-1}^{m-\frac{1}{2}}, \text{NSO}_{k-1}, \phi_{k-1}^n, \psi_{k-1}^n, v).$$

(6) *Compute the coarse grid correction (CGC):*

$$\hat{v}_{1k-1}^m = \hat{c}_{k-1}^m - \bar{c}_{k-1}^m, \quad \hat{v}_{2k-1}^{m-\frac{1}{2}} = \hat{\mu}_{k-1}^{m-\frac{1}{2}} - \bar{\mu}_{k-1}^{m-\frac{1}{2}}.$$

(7) *Interpolate the correction:* $\hat{v}_{1k}^m = I_{k-1}^k \hat{v}_{1k-1}^m$, $\hat{v}_{2k}^{m-\frac{1}{2}} = I_{k-1}^k \hat{v}_{2k-1}^{m-\frac{1}{2}}$.

Here, the coarse values are simply transferred to the four nearby fine grid points, i.e. $v_k(x_i, y_j) = I_{k-1}^k v_{k-1}(x_i, y_j) = v_{k-1}(x_{i+\frac{1}{2}}, y_{j+\frac{1}{2}})$ for i and j odd-numbered integers.

(8) *Compute the corrected approximation on Ω_k*

$$c_k^{m, \text{after CGC}} = \bar{c}_k^m + \hat{v}_{1m}^k, \quad \mu_k^{m-\frac{1}{2}, \text{after CGC}} = \bar{\mu}_k^{m-\frac{1}{2}} + \hat{v}_{2k}^{m-\frac{1}{2}}.$$

(9) *Postsmoothing*

$$\{c_k^{m+1}, \mu_k^{m+\frac{1}{2}}\} = \text{SMOOTH}^v(c_k^n, c_k^{m, \text{after CGC}}, \mu_k^{m-\frac{1}{2}, \text{after CGC}}, \text{NSO}_k, \phi_k^n, \psi_k^n).$$

This completes the description of a nonlinear FAScycle.

We find that convergence of the multigrid method can be achieved with time steps that depend very weakly on the spatial grid size. In particular, convergence is obtained if $\Delta t \approx h$. We define the convergence criterion as a discrete l_2 -norm of the difference between m th and $(m + 1)$ th-iterations becomes less than a tolerance, 10^{-7} . That is,

$$\|c^{m+1} - c^m\| \leq 10^{-7}, \quad \text{where } \|c\| = h \sqrt{\sum_{ij}^{M,N} c_{ij}^2}.$$

The typical number of iterations with the tolerance for the solver to converge is two or three $V(1,1)$ -cycles. For more detailed analysis and notations, see the paper [17]. One should note that there are a couple of differences between the previous paper [17] and this work. First, treatment of nonlinear term, in the previous one, we used a Taylor series expansion, but in this work, we use analytic derivatives. Second, we use a concentration dependent variable mobility here, which was taken as constant in the previous paper. The local mode Fourier analysis for the relaxation step can be done in a similar way as being done in the paper [17].

4.2. Numerical experiments and validation

In this section, we validate our scheme by verifying the second-order convergence, spurious currents, capillary wave, three dimensional drop deformation in a shear flow, Rayleigh-capillary instability, and a rising bubble problem with high density and viscosity ratios.

4.2.1. Convergence test

To obtain an estimate of the rate of convergence, we perform a number of simulations for a sample initial problem on a set of increasingly finer grids. The initial concentration field is

$$c(x,y) = 1 - \frac{1}{2} \left[\tanh \left(\frac{y - 0.25}{2\sqrt{2}\epsilon} \right) + \tanh \left(\frac{0.75 - y}{2\sqrt{2}\epsilon} \right) \right] \quad (31)$$

and initial velocity field is a double shear layer taken from [5]

$$u(x,y) = \begin{cases} \tanh(30(y - 0.25)) & \text{for } y \leq 0.5, \\ \tanh(30(0.75 - y)) & \text{for } y > 0.5, \end{cases}$$

$$v(x,y) = 0.05 \sin(2\pi x),$$

on a square domain, $[0,1] \times [0,1]$. Thus, the initial flow field consists of a horizontal shear layer of finite thickness, perturbed by a small amplitude vertical velocity. The numerical solutions are computed on the uniform grids, $\Delta x = \Delta y = h = 1/2^n$ for $n = 5, 6, 7, 8$, and 9 . For each case, the convergence is measured at time $t = 0.25$ with the uniform time steps, $\Delta t = 0.25h$. The viscosity η is constant and $Re = 100$, $Pe = 10$, and $We = 100$. For the interface parameter ϵ , we want to have smaller ϵ as the grid size h is refined. One possible choice is $\epsilon = O(h^k)$, where k satisfy the condition, $0 < k \leq 1$. Note that k cannot be greater than one because we also want to have a finite number of grid points across interface to accurately calculate surface tension term. For the convergence test, we choose $k = 1/2$, i.e., $\epsilon = 0.02\sqrt{32}h$.

In our formulation of the method for the NSCH equation, since a cell centered grid is used, we define the error to be the discrete l_2 -norm of the difference between that grid and the average of the next finer grid cells covering it:

$$e_{h/\frac{h}{2}} \stackrel{\text{def}}{=} u_{hij} - \left(u_{\frac{h}{2}2i,2j} + u_{\frac{h}{2}2i-1,2j} + u_{\frac{h}{2}2i,2j-1} + u_{\frac{h}{2}2i-1,2j-1} \right) / 4.$$

The rate of convergence is defined as the ratio of successive errors:

$$\log_2(\|e_{h/\frac{h}{2}}\| / \|e_{\frac{h}{4}}\|).$$

In Table 1, the errors and rates of convergence are shown for the velocity components u and v , respectively. Observe that these quantities converge with second order accuracy.

Also in Fig. 5, the time evolution is shown with mesh size 128×128 . In Fig. 6, we plot the interface location on the lower half of the domain with dotted line (32×32), dashed line (64×64), and solid line (128×128). The convergence of the results under grid refinement is evident.

4.2.2. Numerical results on spurious currents

Spurious or parasite currents are described in [30] as vortices “in the neighborhood of interface despite the absence of any external forcing.” They are observed with many surface tension simulation methods including the CSF method. In this section, we test our new surface tension formulation with the similar test problem in [25]. The computational domain is 1×1 and the time step is $\Delta t = 10^{-5}$. The boundary conditions are zero velocity at the top and bottom walls, and periodicity in x -direction. Initially, a circular drop is centered at $(0.5,0.5)$, with radius $a = 0.25$ and surface tension coefficient $\sigma = 0.357$. Both fluids have equal density, 4, and viscosity, 1. The initial velocity field is zero. The exact solution is zero

Table 1
 l_2 -norm of the errors and convergence rates for velocity (u,v)

Case	32–64	Rate	64–128	Rate	128–256	Rate	256–512
u	3.5081e–3	1.89	9.4397e–4	1.99	2.3771e–4	1.95	6.1579e–5
v	1.0145e–4	1.72	3.0805e–5	1.92	8.1282e–6	1.97	2.0742e–6

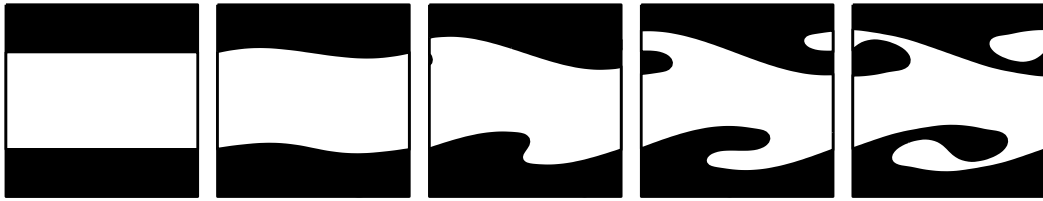


Fig. 5. Evolution of interface from the initial condition (31) with $\epsilon = 0.01$. The times are $t = 0, 0.5, 1.5, 2.5,$ and 5 .

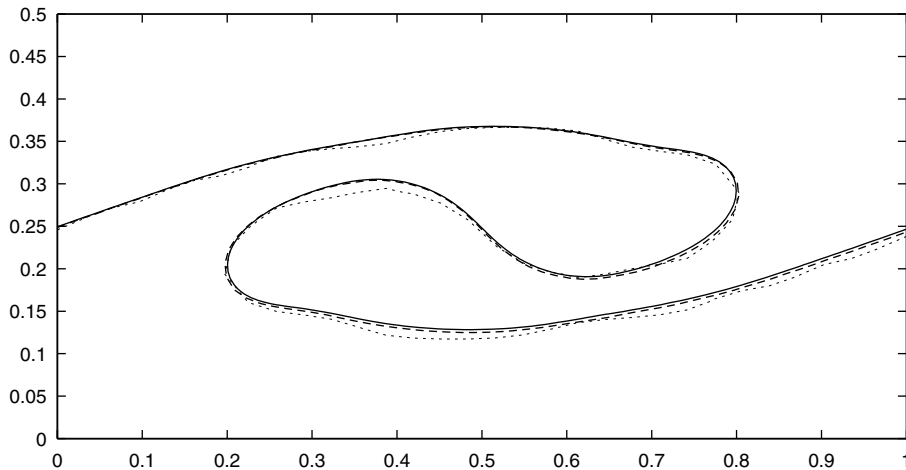


Fig. 6. The interface location on the lower half of the domain. Dotted line 32×32 , dashed line 64×64 , and solid line 128×128 .

velocity for all time. In dimensionless terms, the relevant parameter is the Ohnesorge number $Oh = \eta / \sqrt{\sigma \rho a} \sim 1.6737$.

Table 2 shows three convergence cases of the spurious currents as we refine the mesh size. The first case ($\epsilon = 0.02$) shows almost second order convergence of the spurious velocity when we fix ϵ with refining mesh size. The second case ($\epsilon = 0.02(32h)$) shows minor decreases as we refine the mesh. This is due to the fact that the number of grid points across interface is linearly proportional to ϵ . Therefore, we have same number of grid points across the interface but more grid points tangentially to the interface. The third case ($\epsilon = 0.02\sqrt{32h}$) shows a linear convergence of the spurious currents. This case is between two extreme cases, i.e., the first and the third ones. It does refine interface thickness as the mesh size refines, but compared to fixed ϵ the convergence rate reduces from second to first order.

In Fig. 7, scaled velocity vector, $12000\mathbf{u}$, plots at 200th time step with $\Delta t = 10^{-5}$ are shown. These show the locations of the spurious currents with mesh refinement, $h = 1/32(a)$, $1/64(b)$, and $1/128(c)$ with $\epsilon = 0.02\sqrt{32h}$. The convergence of the spurious currents is evident as we refine the mesh size h and interface parameter ϵ .

4.2.3. Capillary wave

Another important test for the surface tension force is the comparison with the solution of the damped oscillations of a capillary wave. As shown by Prosperetti [23], an analytical solution exists for the initial-value problem in the case of the small-amplitude waves on the interface between two superposed viscous fluids, provided the fluids have the same dynamic viscosity.

Table 2
 l_2 -norm of velocity at 200th time step with $\Delta t = 10^{-5}$

Case	32×32	64×64	128×128	256×256
$\epsilon = 0.02$	$2.8402e-5$	$8.4582e-6$	$2.1636e-6$	$5.7569e-7$
$\epsilon = 0.02(32h)$	$2.8402e-5$	$1.9599e-5$	$1.5097e-5$	$1.3227e-5$
$\epsilon = 0.02\sqrt{32}h$	$2.8402e-5$	$1.3684e-5$	$6.4290e-6$	$3.0879e-6$

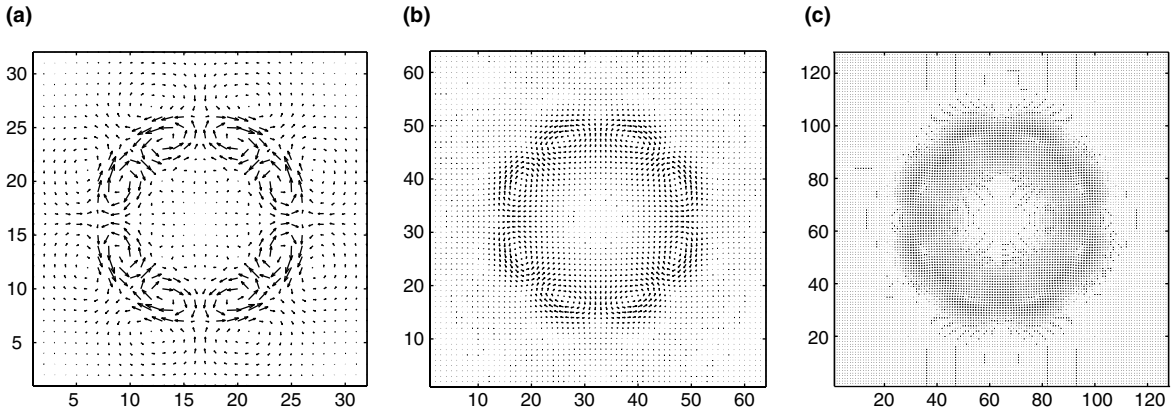


Fig. 7. Scaled velocity vector, $12000\mathbf{u}$, plots at 200th time step with $\Delta t = 10^{-5}$. These show the locations of the spurious currents with mesh refinement, $h = 1/32(a)$, $1/64(b)$, and $1/128(c)$ with $\epsilon = 0.02\sqrt{32}h$. Ticks on each figure are mesh points.

We consider here the case of an initial sinusoidal perturbation of amplitude H_0 and the two fluids being at rest. If ω_0^{-1} is taken as fundamental time with ω_0 given by $\omega_0^2 = \sigma k^3(\rho_1 + \rho_2)$ and k^{-1} as fundamental length, we can set

$$t' = \omega_0 t, \quad \bar{\epsilon} = \nu k^2 / \omega_0.$$

Using these non-dimensional time and viscosity, the analytical solution for the non-dimensional amplitude $a = H/H_0$ is given in compact form by

$$a(t') = \frac{4(1 - 4\beta)\bar{\epsilon}^2}{8(1 - 4\beta)\bar{\epsilon}^2 + 1} \operatorname{erfc}(\sqrt{\bar{\epsilon}t'}) + \sum_{i=1}^4 \frac{z_i \omega_0^2}{Z_i(z_i^2 - \bar{\epsilon}\omega_0)} \exp[(z_i^2 - \bar{\epsilon}\omega_0)t' / \omega_0] \operatorname{erfc}(z_i \sqrt{t' / \omega_0}), \quad (32)$$

where z_i are the four roots of the algebraic equation

$$z^4 - 4\beta\sqrt{\bar{\epsilon}\omega_0}z^3 + 2(1 - 6\beta)\bar{\epsilon}\omega_0z^2 + 4(1 - 3\beta)(\bar{\epsilon}\omega_0)^{3/2}z + (1 - 4\beta)(\bar{\epsilon}\omega_0)^2 + \omega_0^2 = 0 \quad (33)$$

and $Z_1 = (z_2 - z_1)(z_3 - z_1)(z_4 - z_1)$ with Z_2, Z_3, Z_4 obtained by circular permutation of the indices. The dimensionless parameter, β is given by, $\beta = \rho_1\rho_2/(\rho_1 + \rho_2)^2$. For more details about the notations and derivation, see the paper [23].

Now we take a test problem from Zaleski et al. [10]. The computational domain is a unit square box divided in two equal parts by a sinusoidal perturbation. The wavelength is equal to the box width. The boundary conditions are free-slip on the top and bottom walls, periodic along the horizontal axis. The ratio between the initial interface perturbation H_0 and the box height is 0.01. The initial conditions are 128×128 mesh size, $\epsilon = 0.01$, and

$$c(x,y) = \frac{1}{2} \left(1 - \tanh \frac{y - 0.5 - 0.01 \cos(2\pi x)}{2\sqrt{2}\epsilon} \right),$$

$$u(x,y) = v(x,y) = 0.$$

Let $Oh = 1/\sqrt{3000}$, the non-dimensional viscosity $\bar{\epsilon} = \nu k^2/\omega_0 \approx 6.472 \times 10^{-2}$, frequency $\omega_0 = 6.778$, and the two fluid densities are the same.

Fig. 8 shows the evolution of the amplitude with time for the numerical solution (circles) and the initial-value analytical solution (solid line). The numerical results with surface tension formulations (F_1 , F_2 , and F_4) are identical within the tolerance, 10^{-7} . But the numerical calculation blows up in finite time with the formulation F_3 because the chemical potential is not smooth. At early times there is excellent agreement between the theory and simulation. The results slightly deviate when nonlinearity becomes dominant at later times.

In [10], the error is a function of the grid size h and of the initial wave amplitude H_0 . They have studied how varying the grid size h and the ratio h/H_0 influences the convergence toward the analytical solution with a VOF method. When h/H_0 is much larger than 1, the wave amplitude is no longer resolved by the grid and the numerical results diverge. For sufficiently small h , typically from 128^2 to 512^2 , there may be convergence but at a sublinear rate.

4.2.4. Three dimensional drop deformation in a shear flow

We consider a 3D spherical drop in a shear flow. This is a classical problem that was solved analytically for sharp interfaces and small deformations in the creeping flow approximation by Taylor [31]. The drop

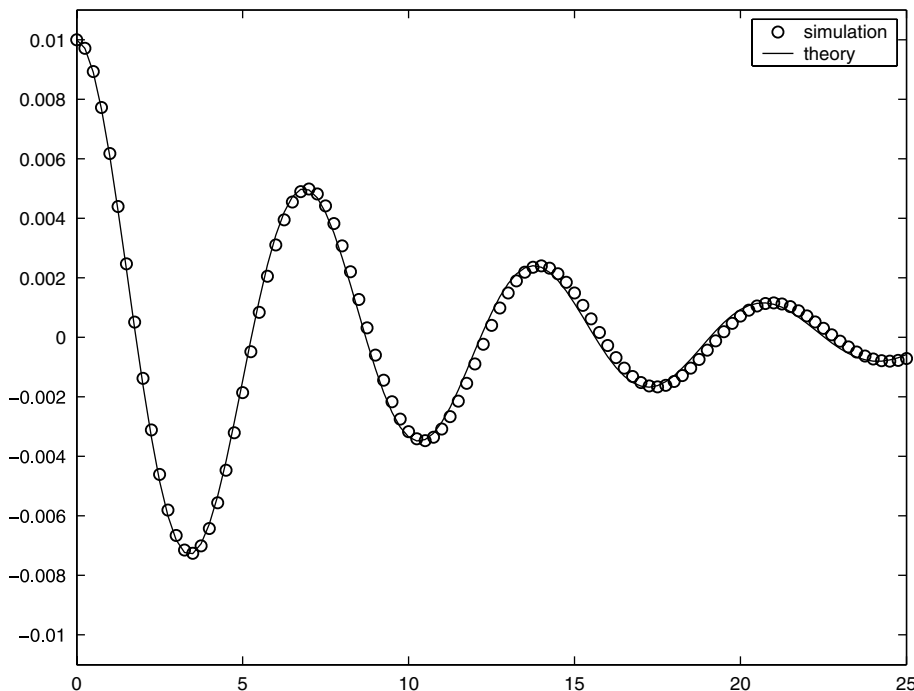


Fig. 8. Time evolution of the amplitude of a capillary wave. The theoretical curve (solid line) is obtained from the exact solution to the initial-value problem in the linearized Navier–Stokes equations.

will assume the shape of an ellipsoid with a deformation that depends on the capillary number and the viscosity ratio.

Taylor [31] found that, when deformation due to the externally imposed shear flow and interfacial relaxation balance one another, the deformation parameter $D = (l - s)/(l + s)$ is related to the capillary number $Ca = \eta\dot{\gamma}a/\sigma$, where $\dot{\gamma}$ is the local shear rate, η is the viscosity of the ambient fluid, a (see Fig. 9(a)) is the drop radius, and σ is the surface tension as

$$D = \frac{19\lambda + 16}{16\lambda + 16} Ca, \quad (34)$$

where l , s (see Fig. 9(b)) and λ denote the longest and shortest axes of the ellipsoid in the shear gradient plane, and the viscosity ratio, respectively. Now we perform 3D simulations with a mesh size $128 \times 64 \times 128$ and a computational domain $\Omega = [-4,4] \times [-2,2] \times [-4,4]$. The initial conditions are

$$c(x,y,z) = \frac{1}{2} \left(1 + \tanh \frac{1 - \sqrt{x^2 + y^2 + z^2}}{2\sqrt{2}\epsilon} \right),$$

$$u(x,y,z) = z, \quad v(x,y,z) = w(x,y,z) = 0, \quad (35)$$

$\dot{\gamma} = 1$, $\lambda = 1$, $\eta = 1$, $\epsilon = 0.04$ and time step $\Delta t = 0.005$ are used.

Fig. 10 shows cross-sectional slice in the x - z plane through the center of the drop for steady-state solution ($Ca = 0.3$) in simple shear along with velocity field. Table 3 shows comparison of Taylor deformation number D obtained by numerical simulations with linear theory. It can be seen that the numerical results are in good agreement with the analytic expression (34).

4.2.5. Axisymmetric immiscible two phase flow: Rayleigh-instability

Surface tension causes the fluid to have as little surface area as possible for a given volume. A long slender column of liquid reduce its surface area by breaking up into a series of small droplets, which have less surface area than the cylinder. This effect is known as the ‘‘Rayleigh instability’’ [24].

We will consider a long cylindrical thread of a viscous fluid 1, the viscosity and density of which are denoted by η_i and ρ_i , respectively, in an infinite mass of another viscous fluid 2 of viscosity η_o and ρ_o . In the unperturbed state, the interface has a perfectly cylindrical shape with a circular cross-section of radius

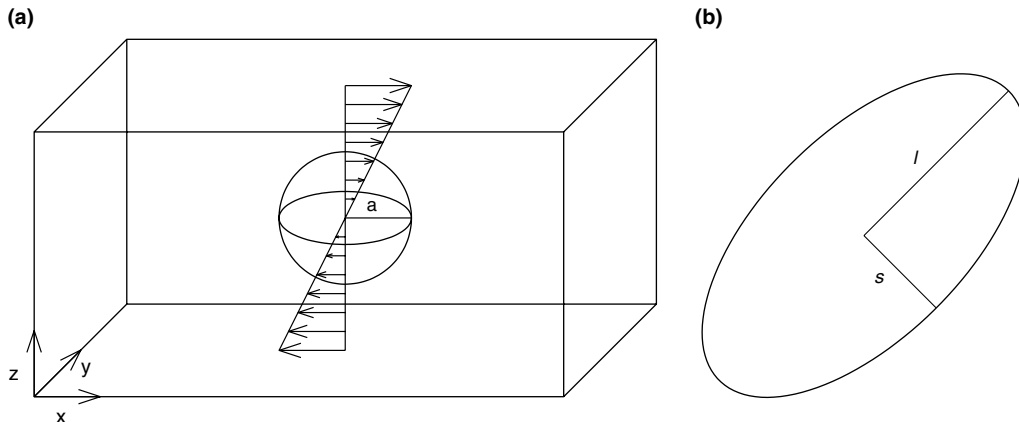


Fig. 9. (a) Schematic of a drop. (b) Schematic of scalar measures of deformation.

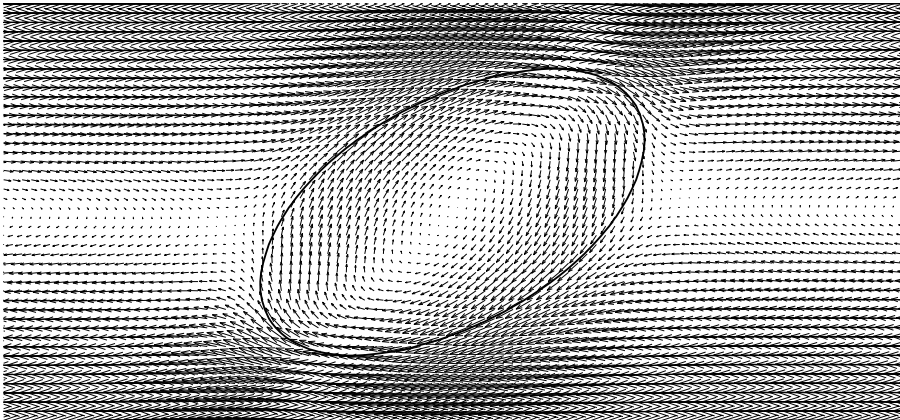


Fig. 10. Cross-sectional slice in the x - z plane through the center of the drop for steady-state solution ($Ca = 0.3$) in simple shear along with velocity field.

Table 3
Comparison of Taylor deformation number D with linear theory

Case	$Ca = 0.1$	$Ca = 0.2$	$Ca = 0.3$
Numerical simulation	0.1143	0.2188	0.3124
Linear theory	0.1094	0.2137	0.3281

a . In this simulation, an initially cosinusoidal perturbation with an amplitude α_0 to the thread radius a is given by

$$R(z) = a + \alpha_0 \cos(kz).$$

In Fig. 11, these parameters are shown schematically. The domain is axisymmetric and the bottom boundary is the axis of symmetry.

The initial concentration field and velocity fields are given by

$$c^0(r,z) = 0.5 \left[1 - \tanh \left(\frac{r - 0.5 - 0.05 \cos(z)}{2\sqrt{2}\epsilon} \right) \right],$$

$$u^0(r,z) = w^0(r,z) = 0$$

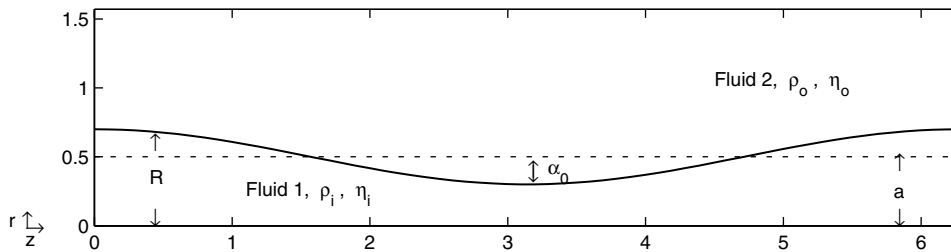


Fig. 11. Schematic of a cylindrical thread of viscous fluid 1 embedded in another viscous fluid 2.

on a domain, $\Omega = \{(r,z) | 0 \leq r \leq \pi \text{ and } 0 \leq z \leq 2\pi\}$. In this computation we use the parameters: $a = 0.5$, $\alpha(0) = 0.05$, $k = 1$, $\epsilon = 0.02$, $Re = 0.32$, $We = 0.032$, $Pe = 1$, and viscosity ratio $\beta = 1$. Mesh size 128×256 and time step $\Delta t = 0.001$ are used. For more detailed description and numerical solution, see [15].

An example of the long time evolution of the interface profile is shown in Fig. 12. In the early states ($t = 0.125$ and 3.125) the surface contour has only one minimum at exactly $z = \pi$. As the time increases, nonlinearities become important and the initially cosinusoidal shape of the interface changes to a more complex form. The zone of the minimum moves symmetrically off the center ($z = \pi$), giving rise to a satellite drop.

In Fig. 13, we plot the $c = 0.5$ contours overlaid with (a) vorticity field and (b) pressure contour lines (higher value in the middle of the thread) at time $t = 3.125$. Positive and negative vorticities are given by solid and dotted curves, respectively. In Fig. 13(b), the pressure field is high in the center of the thread, which forces fluid to move to symmetrically off the center.

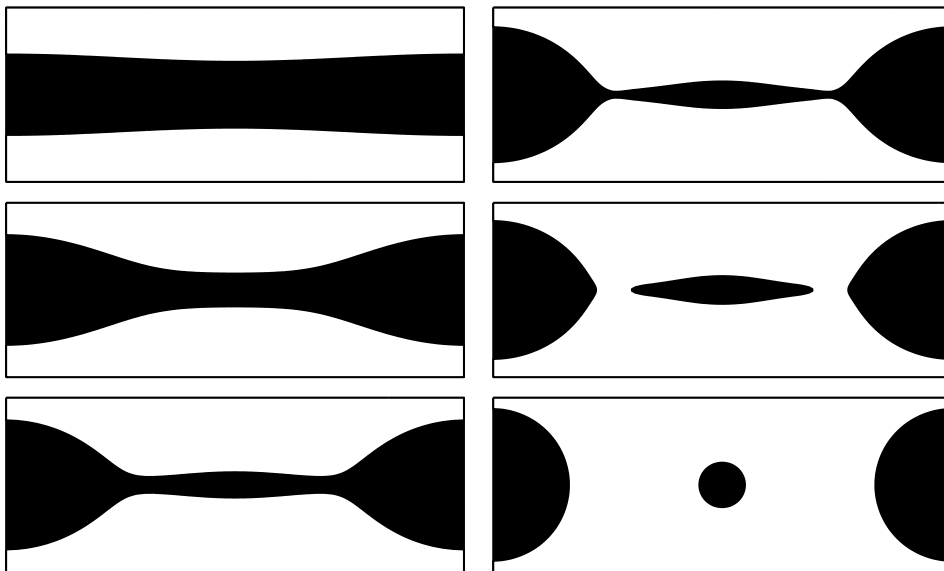


Fig. 12. Time evolution leading to multiple pinch-offs is shown (from top to bottom and left to right). The dimensionless times are at $t = 0.125, 3.125, 4.0, 4.25, 4.375$, and 6.375 . Viscosity ratio is 1, $\epsilon = 0.02$, $Pe = 1$, $Re = 0.32$, and $We = 0.032$.

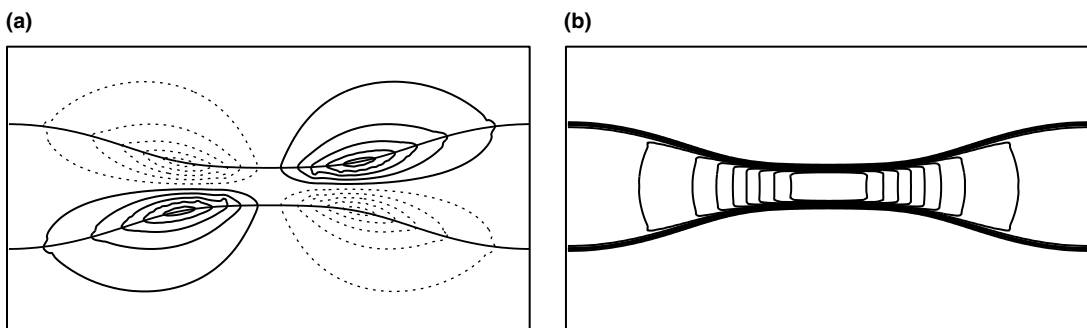


Fig. 13. The $c = 0.5$ contours overlaid with (a) vorticity field and (b) pressure field at time $t = 3.125$.

In Fig. 14, we plot the $c = 0.5$ contours overlaid with (a) vorticity field and (b) pressure contour lines at time $t = 4.0$. In Fig. 14(a), as two minima in the thread develop, the surface tension force produces oppositely signed vortex rings along the interface. This opposite vorticities becomes associated with thread breakup into droplets. This also can be seen from pressure field in Fig. 14(b). Two maxima of pressure field in the off-center positions force the thin thread in the middle to recover to the center, resulting in a satellite droplet.

4.2.6. High density and viscosity ratios variable density and viscosity case

We compute the rise of a gas bubble in liquid to validate the code’s capability for simulating high density and viscosity ratio case. The bubble radius R , the densities of air and water are ρ_{air} and ρ_{water} , respectively. The viscosities are η_{air} and η_{water} .

The nondimensional momentum equations (19) are changed into the following Eqs. (36) to account variable density and viscosity.

$$\mathbf{u}_t + \mathbf{u} \cdot \nabla \mathbf{u} = -\frac{1}{\rho} \nabla p + \frac{1}{\rho Re} \nabla \cdot (\eta(c)(\nabla \mathbf{u} + \nabla \mathbf{u}^T)) - \frac{\epsilon \alpha}{\rho B} \nabla \cdot \left(\frac{\nabla c}{|\nabla c|} \right) |\nabla c| \nabla c + \mathbf{g}, \tag{36}$$

where Bond number $B = 4\rho_{\text{water}}gR^2/\sigma$ and $Re = (2R)^{3/2} \sqrt{g\rho_{\text{water}}}/\eta_{\text{water}}$, and \mathbf{g} represents a unit gravitational force. The nondimensional variable density and viscosity are defined as

$$\rho(c) = (\rho_{\text{air}}c + \rho_{\text{water}}(1 - c))/\rho_{\text{water}}, \quad \eta(c) = (\eta_{\text{air}}c + \eta_{\text{water}}(1 - c))/\eta_{\text{water}}.$$

Fig. 15 shows evolution of a rising bubble with $Re = 100$, $B = 200$, grid 128×256 , $h = \pi/128$, $\epsilon = 0.015$, density ratio $\rho_{\text{water}}/\rho_{\text{air}} = 1000$, and viscosity ratio $\eta_{\text{water}}/\eta_{\text{air}} = 100$. The result with diffuse-interface model qualitatively compares well to the results from level set method [29].

5. Discussion and conclusion

A new surface tension force formulation for diffuse-interface models has been derived for incompressible, immiscible Navier–Stokes equations separated by an interface. The new formulation allows us to calculate pressure field directly from the governing equations. Numerical experiments have been presented to demonstrate the accuracy and effectiveness of the method. The results showed that the method is promising in the numerical simulation of two-phase fluid flows.

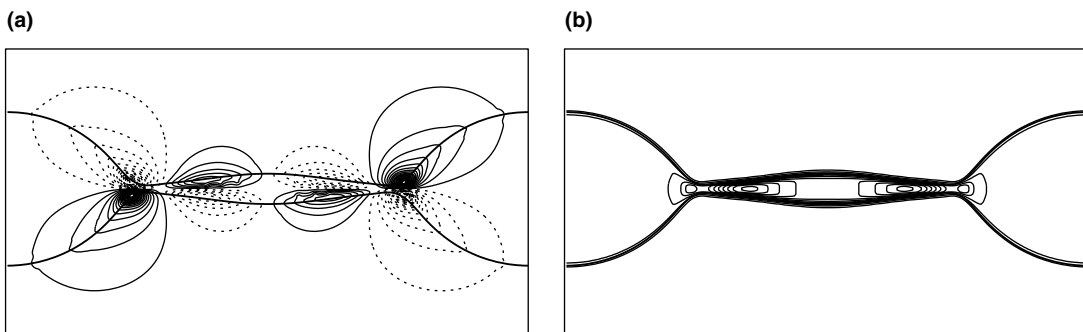


Fig. 14. The $c = 0.5$ contours overlaid with (a) vorticity field and (b) pressure field at time $t = 4.0$.

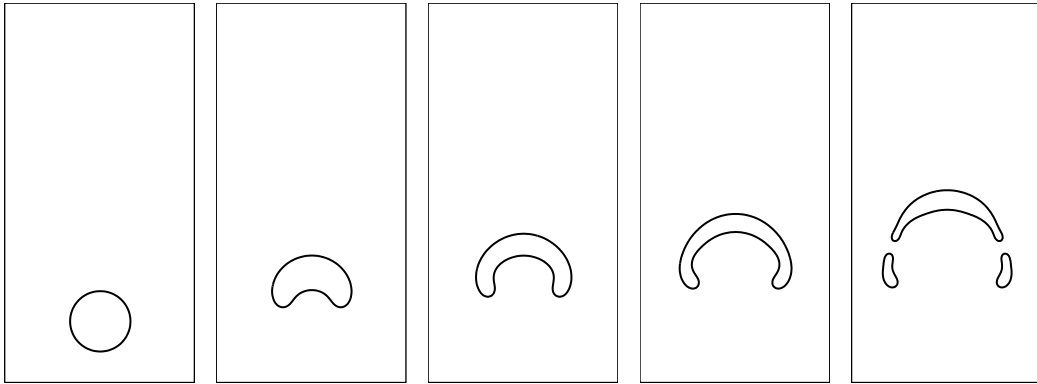


Fig. 15. Evolution of rising bubble with $Re = 100$, $B = 200$, grid 128×256 , $h = \pi/128$, $\epsilon = 0.015$, density ratio $\rho_{\text{water}}/\rho_{\text{air}} = 1000$, and viscosity ratio $\eta_{\text{water}}/\eta_{\text{air}} = 100$. Time increases from left to right ($t = 0, 2.1, 3.0, 3.9, \text{ and } 5.1$).

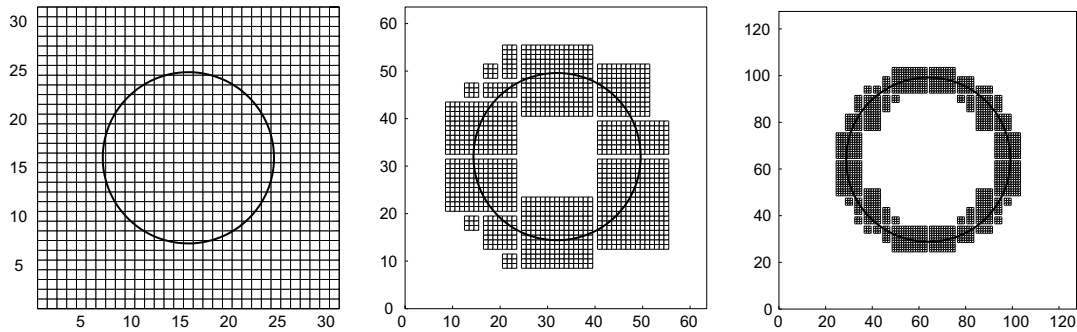


Fig. 16. Adaptive mesh refinement.

In the future, we would like to incorporate adaptive mesh refinement method into the diffuse-interface method. When we solve fluid flow problems with moving interfaces numerically, high grid resolution is needed to adequately solve the equations. However, there are often also large portions of the domain where high levels of refinement are not needed; using a highly refined mesh in these regions represents a waste of computational effort. By locally refining the mesh only where needed, Adaptive Mesh Refinement (AMR) allows concentration of effort where it is needed, allowing better resolution of the problem. Fig. 16 illustrates this concept. We recursively refine the mesh around the interface to resolve interfacial area and put most of computational load on that region. Currently, we are developing AMR diffuse-interface model for an incompressible two-phase fluid flow system using the adaptive framework [1] from “The Center for Computational Sciences and Engineering at Lawrence Berkeley National Laboratory”.

Acknowledgements

The author thanks his advisor, John Lowengrub, for intellectual and financial support. This work was supported by the National Science Foundation, Division of Mathematical Sciences and the Department of

Energy, Basic Energy Sciences Division. The author acknowledges the support of the Network and Academic Computing Services (NACS) at the University of California, Irvine.

References

- [1] A.S. Almgren, J.B. Bell, P. Colella, L.H. Howell, M.L. Welcome, A conservative adaptive projection method for the variable density incompressible Navier–Stokes equations, *J. Comput. Phys.* 142 (1998) 1–46.
- [2] D.M. Anderson, G.B. McFadden, A.A. Wheeler, Diffuse-interface methods in fluid mechanics, *Ann. Rev. Fluid Mech.* 30 (1998) 139–165.
- [3] F. Boyer, A theoretical and numerical model for the study of incompressible mixture flows, *Comput. Fluids* 31 (2002) 41–68.
- [4] V.E. Badalassi, H.D. Ceniceros, S. Banerjee, Computation of multiphase systems with phase field models, *J. Comput. Phys.* 190 (2003) 371–397.
- [5] J. Bell, P. Colella, H. Glaz, A second-order projection method for the incompressible Navier–Stokes equations, *J. Comput. Phys.* 85 (2) (1989) 257–283.
- [6] J.U. Brackbill, D.B. Kothe, C. Zemach, A continuum method for modeling surface tension, *J. Comput. Phys.* 100 (1992) 335–354.
- [7] Y.C. Chang, T.Y. Hou, B. Merriman, S. Osher, A level set formulation of eulerian interface capturing methods for incompressible fluid flows, *J. Comput. Phys.* 124 (1996) 449–464.
- [8] J.W. Cahn, J.E. Taylor, Surface motion by surface diffusion, *Acta Metall.* 42 (1994) 1045–1063.
- [9] R. Chella, J. Viñals, Mixing of a two-phase fluid by cavity flow, *Phys. Rev. E* 53 (1996) 3832–3840.
- [10] D. Gueyffier, Jie Li, Ali Nadim, R. Scardovelli, S. Zaleski, Volume-of-fluid interface tracking with smoothed surface stress methods for three-dimensional flows, *J. Comput. Phys.* 152 (1999) 423–456.
- [11] D. Gao, N.B. Morley, V. Dhir, Numerical simulation of wavy falling film flow using VOF method, *J. Comput. Phys.* 192 (2003) 624–642.
- [12] M.E. Gurtin, D. Polignone, J. Viñals, Two-phase binary fluids and immiscible fluids described by an order parameter, *Math. Models Meth. Appl. Sci.* 6 (6) (1996) 815–831.
- [13] D. Jacqmin, Calculation of two-phase Navier–Stokes flows using phase-field modeling, *J. Comput. Phys.* 155 (1999) 96–127.
- [14] D. Jacqmin, Contact-line dynamics of a diffuse fluid interface, *J. Fluid Mech.* 402 (2000) 57–88.
- [15] Junseok Kim, A diffuse-interface model for axisymmetric immiscible two-phase flow, *Appl. Math. Comput.* 160 (2005) 589–606.
- [16] H. Kodama, M. Doi, Shear-induced instability of the lamellar phase of a block copolymer, *Macromolecules* 29 (1996) 2652–2658.
- [17] Junseok Kim, Kyungkeun Kang, J. Lowengrub, Conservative multigrid methods for Cahn–Hilliard fluids, *J. Comput. Phys.* 193 (2004) 511–543.
- [18] Junseok Kim and John Lowengrub, Ternary Cahn–Hilliard fluids, submitted for publication.
- [19] H.Y. Lee, J.S. Lowengrub, J. Goodman, Modeling pinchoff and reconnection in a Hele–Shaw cell. I. The models and their calibration, *Phys. Fluids* 14 (2) (2002) 492–513.
- [20] H.Y. Lee, J.S. Lowengrub, J. Goodman, Modeling pinchoff and reconnection in a Hele–Shaw cell. II. Analysis and simulation in the nonlinear regime, *Phys. Fluids* 14 (2) (2002) 514–545.
- [21] Chun Liu, Jie Shen, A phase field model for the mixture of two incompressible fluids and its approximation by a Fourier-spectral method, *Physica D* 179 (2003) 211–228.
- [22] J.S. Lowengrub, L. Truskinovsky, Quasi-incompressible Cahn–Hilliard fluids and topological transitions, *Proc. R. Soc. Lond. A* 454 (1998) 2617–2654.
- [23] A. Prosperetti, Motion of two superposed viscous fluids, *Phys. Fluids* 24 (1981) 1217–1223.
- [24] W.S. Rayleigh, On the instability of jets, *Proc. London Math. Soc.* 10 (1878) 4–13.
- [25] Y.Y. Renardy, M. Renardy, PROST: a parabolic reconstruction of surface tension for the volume-of-fluid method, *J. Comput. Phys.* 183 (2002) 400–421.
- [26] Y.Y. Renardy, M. Renardy, V. Cristini, A new volume-of-fluid formation for surfactants and simulations of drop deformation under shear at a low viscosity ratio, *Eur. J. Mech. B/Fluids* 21 (2002) 49–59.
- [27] V.N. Starovoitov, Model of the motion of a two-component liquid with allowance of capillary forces, *J. Appl. Mech. Techn. Phys.* 35 (1994) 891–897.
- [28] C.W. Shu, S. Osher, Efficient implementation of essentially non-oscillatory shock capturing schemes II, *J. Comput. Phys.* 83 (1989) 32–78.
- [29] M. Sussman, P. Smereka, S. Osher, A level set approach for computing solutions to incompressible two-phase flow, *J. Comput. Phys.* 114 (1994) 146–159.
- [30] R. Scardovelli, S. Zaleski, Direct numerical simulation of free surface and interfacial flow, *Annu. Rev. Fluid Mech.* 31 (1999) 567–603.
- [31] G.I. Taylor, The deformation of emulsions in definable fields of flows, *Proc. R. Soc. Lond. A* 146 (1934) 501–523.

- [32] Hao Tang, L.C. Wrobel, Z. Fan, Tracking of immiscible interfaces in multiple-material mixing processes, *Comp. Mater. Sci.* 29 (2004) 103–118.
- [33] U. Trottenberg, C. Oosterlee, A. Schüller, *Multigrid*, Academic Press, New York, 2001.
- [34] M. Verschuere, F.N. Van De Vosse, H.E.H. Heijer, Diffuse-interface modelling of thermocapillary flow instabilities in a Hele–Shaw cell, *J. Fluid Mech.* 434 (2001) 153–166.
- [35] K. Yokoi, Feng Xiao, Mechanism of structure formation in circular hydraulic jumps: numerical studies of strongly deformed free-surface shallow flows, *Physica D* 161 (2002) 202–219.
- [36] X. Zheng, S.M. Wise, V. Cristini, Nonlinear simulation of tumor necrosis, neo-vascularization and tissue invasion via an adaptive finite-element/level-set method, *Bull. Math. Biol.*, in press.